

# Implanted Battery-Free Direct-Current Micro-Power Supply from in Vivo Breath Energy Harvesting

Jun Li,<sup>†,‡,#</sup> Lei Kang,<sup>‡,§,#</sup> Yin Long,<sup>†,||</sup> Hao Wei,<sup>‡,⊥</sup> Yanhao Yu,<sup>†</sup> Yizhan Wang,<sup>†</sup> Carolina A. Ferreira,<sup>‡</sup> Guang Yao,<sup>†,||</sup> Ziyi Zhang,<sup>†</sup> Corey Carlos,<sup>†</sup> Lazarus German,<sup>†</sup> Xiaoli Lan,<sup>⊥</sup> Weibo Cai,<sup>\*,†,‡,¶</sup> and Xudong Wang<sup>\*,†,‡</sup>

<sup>†</sup>Department of Materials Science and Engineering, University of Wisconsin–Madison, Madison, Wisconsin 53706, United States

<sup>‡</sup>Department of Radiology and Medical Physics, University of Wisconsin–Madison, Madison, Wisconsin 53705, United States

<sup>§</sup>Department of Nuclear Medicine, Peking University First Hospital, Beijing 100034, China

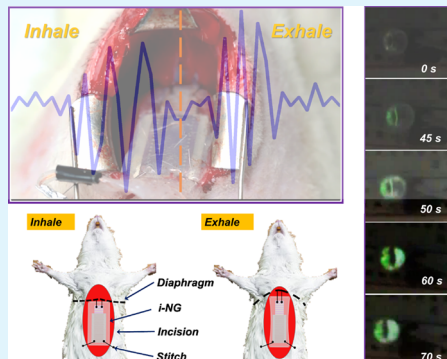
<sup>||</sup>State Key Laboratory of Electronic Thin Films and Integrated Devices, School of Optoelectronic Information, University of Electronic Science and Technology of China (UESTC), Chengdu 610054, China

<sup>⊥</sup>Department of Nuclear Medicine, Union Hospital, Tongji Medical College, Huazhong University of Science and Technology, Wuhan 430022, China

## Supporting Information

**ABSTRACT:** In vivo biomechanical energy harvesting by implanted nanogenerators (i-NGs) is promising for self-powered implantable medical devices (IMDs). One critical challenge to reach practical applications is the requirement of continuous direct-current (dc) output, while the low-frequency body activities typically generate discrete electrical pulses. Here, we developed an ultra-stretchable micrograting i-NG system that could function as a battery-free dc micro-power supply. Packaged by a soft silicone elastomer with a cavity design, the i-NG exhibited an ultralow Young's modulus of ~45 kPa and a high biocompatibility to soft biological tissues. The i-NG was implanted inside the abdominal cavity of Sprague Dawley adult rats and directly converted the slow diaphragm movement during normal respiration into a high-frequency alternative current electrical output, which was readily transmitted into a continuous ~2.2 V dc output after being integrated with a basic electrical circuit. A light-emitting diode was constantly operated by the breath-driven i-NG without the aid of any battery component. This solely biomechanical energy-driven dc micro-power supply offers a promising solution for the development of self-powered IMDs.

**KEYWORDS:** *implantable nanogenerator, energy harvesting from respiration, implantable medical devices, battery-free system, direct-current micro-power source*



## INTRODUCTION

The rapid advancement of implantable medical devices (IMDs) is revolutionizing the healthcare industry nowadays.<sup>1–3</sup> As modern IMDs being made smaller, lighter, safer, and more effective and durable owing to the technology revolution of microelectronics, their electrical power source, however, appeared to be a more and more serious limitation for future device development. Majority of current IMDs are powered by conventional primary or secondary batteries that contribute up to 90% weight and volume of the entire device.<sup>4,5</sup> Replacement of or recharging the batteries requires substantial surgical or technical efforts, introducing additional suffering and complexity to the patients. Besides, other potential issues related to batteries such as overheat induced by mechanical stress and leakage of toxic electrolyte further prohibit the advancement and miniaturization of IMDs. Therefore, increasing efforts are now being focused on the

innovation of designated IMD power sources that are biocompatible, biosafe, flexible, and with a longer lifetime.

Most IMDs have a power requirement at the micro to milliwatts scale (Table S1). For instance, the state-of-the-art pacemaker has a power consumption of 5–10  $\mu\text{W}$ .<sup>6</sup> Considering that the human body is a rich source of energy with average stored energy equivalent to 3 V battery with approximately 55 000 A·h capacity (Supporting Information S3),<sup>7–9</sup> energy harvested from body motions, heat, and body fluids can be quite sufficient for the operation of IMDs and thereby enables self-powered capability bypassing the requirement of batteries. So far, various energy harvesters that operate either *in vitro*<sup>6,10,11</sup> or *in vivo*<sup>6,12–15</sup> have been demonstrated.

Received: September 12, 2018

Accepted: November 16, 2018

Published: November 16, 2018

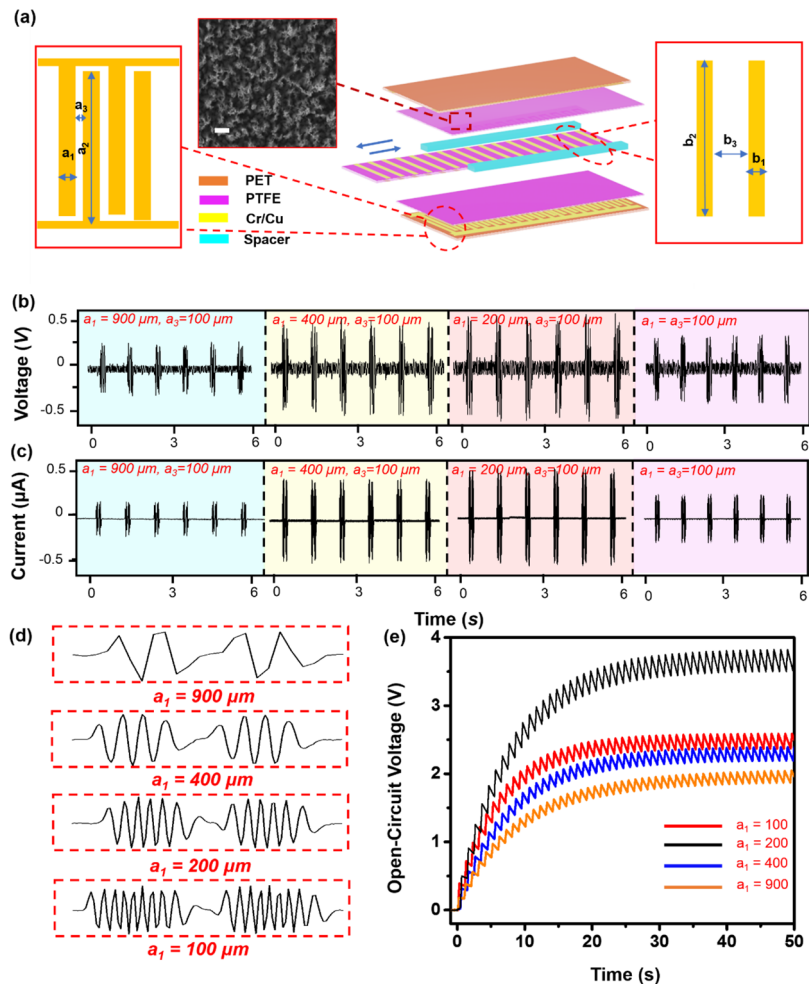


**Figure 1.** Nanogenerator design and electrical output characterization. (a) Schematic diagram showing the in-plane sliding mode of a triboelectric nanogenerator. The middle inset is a scanning electron microscopy image of the nanostructured PTFE surface. Scale bar is 1  $\mu\text{m}$ . The left and right insets show the electrode design and geometric parameters. (b,c) Voltage (b) and short-circuit current (c) outputs of the triboelectric nanogenerator with different electrode finger widths, when they were stretched to the same displacement of 4 mm at 1 Hz frequency. (d) Enlarged current output profiles during one sliding cycle. (e) Voltage measured on a 0.1  $\mu\text{F}$  capacitor when charged by the four different NGs.

As an example, the electromagnetic energy harvester has appreciable outputs from several microwatts to hundreds of milliwatts when driven by the vibration stimulation with difference frequencies<sup>11,15</sup> and exhibits promising potential to serve as power supply for various IMDs.<sup>16</sup> Meanwhile, implantable nanogenerators (i-NGs) based on the principle of either triboelectric (TENG)<sup>17–22</sup> or piezoelectric<sup>12,23,24</sup> have been designed to convert biomechanical energy into electricity. Compared to other technologies, such as implantable thermoelectric generator and electromagnetic generator, i-NGs are highly efficient, flexible, and lightweight, exhibiting excellent compatibility to tissues and organs. Nevertheless, unlike other mechanical energy sources, nearly all body activities, such as heart beat, breathing, and muscle stretching, are resident at the low-frequency regime (<5 Hz). Therefore, the outputs of state-of-the-art i-NGs are always in a form of largely discrete pulses which are impractical as direct power sources.<sup>23,25,26</sup> Although their theoretical output power (instant power reached up to 20  $\mu\text{W}$  when implanted on pig's heart<sup>27</sup>) could be sufficient for IMDs, the battery component is still needed in the i-NG design to produce a steady useable direct current (dc) output. Moreover, a large mismatch in the mechanical properties still exists between the

i-NG polymer film and soft biological tissues (e.g., the commonly used Kapton film without any specific structure design has a Young's modulus of 2–5 GPa<sup>28,29</sup>), which inevitably leads to low energy conversion efficiency as well as multiple side effects to the host.

Among the several TENG operation modes, the sliding mode based on grating electrodes bestows NG with the unique capability of frequency transforming. It could be a good solution for converting slow biomechanical motions into continuous electric signals. In this work, we reported an ultrasoft and stretchable i-NG system with a tissue-comparable Young's modulus, which could function as a battery-free dc micro-power supply. Because of the central-cavity package design, the i-NG exhibited an extremely low Young's modulus (~45 kPa) that matches most soft tissues in the body (5–100 kPa). Additionally, the design of microscale interdigital electrodes (IDEs) enabled an effective transformation of slow linear motion into a high-frequency sinusoidal output. The output power could be further improved by implementing multiple tribo-active layers. When implanted inside the abdominal cavity of Sprague Dawley (SD) adult rats, the i-NG successfully converted the slow diaphragm movement during normal breath into high-frequency electric signals,

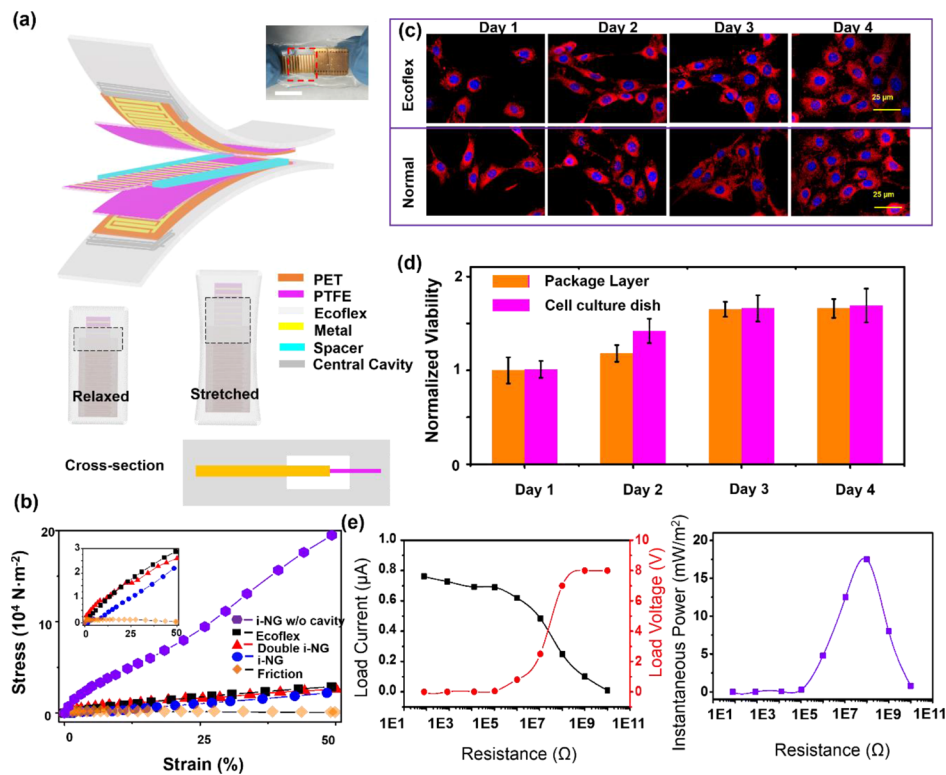


**Figure 2.** I-NG design and characterization. (a) Schematic diagram showing the packaging configuration of an i-NG. The inset is a digital image of a packaged i-NG that was stretched. The scale bar is 1 cm. (b) Strain and stress curves of the i-NG without a central cavity design (violet hexagon), the pure Ecoflex material (black squares), i-NG devices with a double triboelectric unit (red triangles) and single unit (blue dots), and an unpackaged triboelectric pair (orange diamonds). The inset is an enlarged figure of curves concentrated at lower stress. (c) Fluorescence microscope image of 3T3 fibroblast cells stained by Texas Red-X phalloidin and Hoechst. (d) Cell viability as a function of time. (e) Left panel is the output voltage and current dependence of the i-NG on the load resistance at a frequency of 1 Hz and at a low driven speed of 4 cm/s. The right panel is the calculated instantaneous output power with respect to the resistance load.

which were readily transmitted into a continuous  $\sim 2.2$  V dc output on a light-emitting diode (LED) load after being integrated with a basic electrical circuit (rectifier and capacitor). This work distinguishes from previous arts of *in vivo* energy harvesting (*Supporting Information* Table S2), such as the breathing energy harvesting by Zheng et al.<sup>21</sup> in terms of the i-NG design, enhanced high-frequency electrical output, and biologically comparable mechanical property. This direct *in vivo* conversion of biomechanical energy into useful electricity for continuous operation of small electronics demonstrated a successful battery-free technology for self-powered IMD systems.

## RESULTS AND DISCUSSIONS

**Micrograting Nanogenerator Design and Characterization.** Finer grating shortens the time to transport induced charges between the electrodes, resulting in higher output current and larger amount of transported charge with fixed dimension and at constant velocity. A micrograting TENG electrode was therefore selected and designed to achieve a desired magnitude and frequency of electric output.<sup>30,31</sup> As presented in Figure 1a, the TENG had a multilayered structure, including two symmetric electrode layers (top and bottom layer) and one mobile layer for electrification (middle layer). Each electrode layer consisted of Cu/Cr IDEs deposited on a flexible polyethylene terephthalate (PET) substrate (50  $\mu$ m thickness) and covered by a thin layer of polytetrafluoro-

ethylene (PTFE) (50  $\mu$ m). Individual fingers of IDEs had a width of  $a_1$  (100–900  $\mu$ m) with a length of  $a_2$  (1 cm) and separated by a gap of  $a_3$  (100  $\mu$ m). Dense nanowire arrays were created on the surface of PTFE by the inductively coupled plasma (ICP) to further enhance the contact area and surface charge density.<sup>32,33</sup> The middle mobile layer was composed of a central PET film (50  $\mu$ m) sandwiched between two PTFE films (50  $\mu$ m). Cu/Cr metal strips were deposited on the PTFE film. The detailed fabrication process is included in Figure S1.

To investigate the electrode geometry-related electrical output, four TENGs with IDE finger widths of  $a_1 = 900$ , 400, 200, and 100  $\mu$ m at a fixed gap ( $a_3 = 100 \mu\text{m}$ ) (Figure S2) were evaluated. The width ( $b_1$ ) and gap ( $b_3$ ) of metal strips in the middle layer were reconfigured accordingly following the relations:  $a_1 = b_1$  and  $b_3 = 2a_3 + a_1$ . The length ( $b_2$ ) has a constant value of 0.8 cm. Matching of the periodicities of IDEs and metal strips is essential for maximizing the output (details elaborated in Figure S3). The TENG outputs were measured by sliding the middle layer back and forth at a constant low velocity of 4 cm/s mimicking the motion of the diaphragm. The relative displacement between the two sets of electrodes was kept at 4 mm. As shown in Figure 1b, the highest peak-to-peak voltage ( $V_{pp}$ ) was  $\sim 800$  mV from the TENGs with electrode widths of 400 and 200  $\mu$ m. The device with the largest electrode width of 900  $\mu$ m yielded the lowest output of 300 mV. Although the 100  $\mu$ m electrode width design enabled the densest output peaks, relatively low voltages were obtained

( $V_{pp} \approx 500$  mV). Short-circuit currents ( $I_{sc}$ ) were measured from the four TENGs under the same mechanical displacement conditions. A similar trend of  $I_{sc}$  change was observed in correlation with the electrode width. The highest peak-to-peak  $I_{sc}$  of  $\sim 0.9 \mu\text{A}$  was obtained from the 400 to 200  $\mu\text{m}$  electrodes, whereas the 900  $\mu\text{m}$  electrodes yielded the lowest  $I_{sc}$  of  $\sim 0.3 \mu\text{A}$  (Figure 1c). The best performed 200  $\mu\text{m}$  electrode design could be attributed to the optimal surface area for charge collection and balanced dielectric gap spacing for charge transfer.<sup>34,35</sup> Specifically, as the electrode width decreases, the number of electrodes in the same area would increase, shortening the time of charge transfer and thus enhancing the electric output. However, increasing the number of electrodes would decrease the total electrode area (given the gaps between each two electrode fingers being kept constant), which would reduce the electric output because of the less effective area and less amount of transferred charge. Same as the voltage outputs, each back-and-forth sliding generated a pair of current peak envelops. The number of current peaks within each envelop was directly related to the number of electrodes being interacted (Figure 1d). Take the 200  $\mu\text{m}$  electrode design as an example, seven peaks were generated within one envelope of 0.1 s, corresponding to a frequency of 70 Hz. The current profile within each envelope was close to a sinusoidal curve, demonstrating a successful conversion of slow linear motion into a continuous high-frequency electrical output. Although the individual current peak was slightly low (average  $\approx 0.6 \mu\text{A}$ ), the large number of current peaks ensured a largely enhanced charge generation.

The micrograting TENGs were then utilized to charge a small capacitor to investigate their potential as an effective power supply in terms of electrical energy generation. The TENG was connected to a capacitor (0.1  $\mu\text{F}$ ) through a regular rectification bridge circuit (equivalent circuit is shown in Figure S4), and the charging results are shown in Figure 1d. The NG with 200  $\mu\text{m}$  electrodes yielded the fastest capacitor charging behavior and reached a voltage of 2.5 V in 10 s. Although the 100  $\mu\text{m}$  electrode NG had the highest frequency when driven by the same motion, its much lower amplitude (maximum  $\sim 0.5 \mu\text{A}$ ) yielded a slightly lower charging rate on the same capacitor. The even slower charging rates from the 400 to 900  $\mu\text{m}$  electrode designs were primarily because of their low current peak frequencies.

#### Stretchable and Implantable TENG Development.

The best-performed 200  $\mu\text{m}$  electrode design was selected for i-NG integration and testing. To make the TENG implantable, the entire device was packaged by Ecoflex 00-30 to prevent the biofluids and electrical leakage. Ecoflex is a soft silicone elastomer with a low Young's modulus of  $\sim 60$  kPa and a high elasticity (900% strain at break) and has been widely used for soft electronics and artificial muscle designs.<sup>36–38</sup> The schematic configuration of the packaged i-NGs is shown in Figure 2a, and the detailed fabrication procedures are given in the Supporting Information Figure S1. After NG was packaged, the *in vitro* output was first evaluated on different load resistances driven by a slow linear motion of 4 cm/s at a frequency of 1 Hz (Figure 2e). It exhibited a short-circuit current (peak to peak) of 0.8  $\mu\text{A}$  and an open-circuit voltage (peak to peak) of 8 V with a maximum instantaneous power around 20 mW/m<sup>2</sup> at 10 M $\Omega$ . Afterward, the mechanical property of the as-fabricated i-NG was characterized by a dynamic mechanical analyzer and compared to the pure Ecoflex elastomer with the same thickness. The corresponding

stress-strain curves are shown in Figure 2b. Within 50% strain (1.5 cm elongation), the Young's modulus of the device was estimated to be  $\sim 46$  kPa, even lower than that of pure Ecoflex ( $\sim 67$  kPa). The low Young's modulus could be attributed to the central cavity (1.2 cm  $\times$  1.8 cm) inside i-NGs, which was vital to allow relatively free sliding of the middle piece. Without this central cavity, because of the Poisson effect, the elongated device will have certain transverse contraction, which, however, was significantly impeded by the embedded rigid NG, leading to a 10-time higher Young's modulus ( $\sim 0.4$  MPa). The central cavity not only reduced the amount of Ecoflex per unit cross-sectional area and thus less tensile strain compared to a solid Ecoflex piece with the same geometry but also allows lateral shrinkage of the elastomer package when stretched moderately. Given the negligibly small contribution from the friction between the center piece and the electrode layers (orange diamonds in Figure 2b), an overall less strain was obtained from the packaged i-NG. The negligible strain contribution from the sliding thin film allowed an integration of multitribolayers with minimal increase of the overall Young's modulus. To test this hypothesis, the TENG active component was made of two units of the 200  $\mu\text{m}$  electrode pairs (Figure S5). The electric output was nearly doubled compared to the i-NG with a single unit (0.8 V) and reached 1.6 V (Figure S5d). Meanwhile, the device Young's modulus only increased to 52 kPa (Figure 2b). Because the elastic modulus of most soft tissues is in the range of 5–200 kPa,<sup>39–41</sup> this ultrastretchable i-NG is expected to exhibit an excellent compatibility to interface biological tissues. More mechanical properties of as-prepared i-NG are included in Supporting Information as Figure S6.

To further verify the biocompatibility of the Ecoflex package, the viability of 3T3 fibroblast cells was examined on top of the Ecoflex film. Fluorescence microscopy revealed that the cell morphology on Ecoflex exhibited no difference when compared to those growing on standard tissue culture plates over 4 days (Figure 2c). 3-(4,5-Dimethylthiazol-2yl)-2,5-diphenyl-2H-tetrazolium bromide (MTT) assay was performed to evaluate the cellular metabolic activity as a reference for cell growth/proliferation (Figure S7). As shown by the statistic measurements in Figure 2d, the cell viability on Ecoflex did not exhibit significant difference (<2%) compared to the control group, confirming the nontoxicity of Ecoflex package materials. The good biocompatibility discovered from Ecoflex was consistent with other literature reports.<sup>42,43</sup>

The continuous high-frequency ac signal enabled an effective transformation of the i-NG output into a dc signal through a simple rectifier and a capacitor circuitry (right inset of Figure 3a). Driven by a linear motor, the i-NG was stretched at a velocity of 4 cm/s to an extension of 4 mm at a frequency of 1 Hz to simulate the diaphragm motion during breath. A green LED was connected to the two electrodes of the capacitor as a load. Under this condition, the voltage of the capacitor (0.33  $\mu\text{F}$ ) continually built up at the first 25 s and reached a constant value of  $\sim 2.2$  V on the LED load (left inset of Figure 3a). Accordingly, the LED was gradually lighted up in the first 25 s and reached its full brightness following the voltage buildup trend (Figure 3b). The LED remained at the on state constantly as long as the slow stretching motion was in action (Video S1). The voltage output was kept at the  $\sim 2.2$  V level on the LED load during the entire 120 min testing period (Figure 3a), evidencing that the i-TENG could be readily used as a dc power source same as a regular battery without involving any

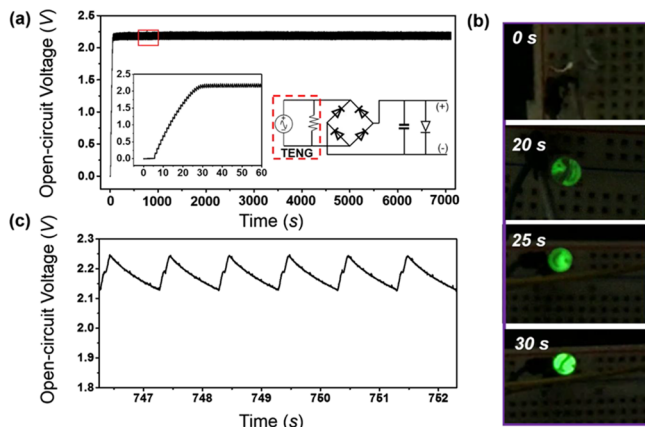


**Figure 3.** In vitro power generating performance. (a) Long-term open-circuit potential recorded at a green LED load powered by a packaged i-NG. Left inset: The first 1 min charging curve on the LED load; Right inset: Schematic circuit design. (b) Series of images recorded on the LED showing the lighting process as the voltage is building up. (c) Zoomed-in voltage profile at the flat region in the red box in (a).

toxic chemicals. The zoomed-in voltage curve at the flat region showed a triangular profile with a peak-to-peak difference of  $\sim 130$  mV (Figure 3c). This small drop was a result of the discharge through the LED load. It confirmed that the capacitor charging through i-NG could completely compensate

the power drain from the electronic load. The average dc output power was determined to be a constant  $0.12 \mu\text{W}$  on the LED load during the testing period from the charging and discharging curve (detailed calculation process was provided in the Supporting Information, S2). Therefore, given the sub microwatt-level power consumption for typical sensing nodes, this micro-power supply could continuously support the operation of these electronic IMDs driven by the slow stretching motion.

The i-NG was then implanted in SD adult rats ( $\sim 500$  g) to investigate its in vivo energy generation performance. Packaged i-NGs with the  $200 \mu\text{m}$  electrode design were implanted inside the abdominal cavity by fixing one end at the diaphragm muscle near the central tendon part while the other end was stitched to the abdominal wall (Figure 4a). The detailed implantation procedure is given in Figure S8. The i-NG has a similar mechanical property as the rat diaphragm muscle which usually has a Young's modulus of  $50\text{--}70$  kPa.<sup>44,45</sup> During normal breath, the up and down movement of the diaphragm would create periodic stretching and relaxing motions on the i-NG (Video S2). Specifically, during exhalation, the lung recoils to force the air out and the diaphragm relaxes toward a higher position in the thoracic cavity, stretching the i-NG [Figure 4b(i)]. During inhalation, the diaphragm contracts and moves toward the inferior direction and thus relaxes the i-NG [Figure 4b(ii)]. Such a periodic motion enabled the relative sliding of the i-NG electrodes and produced groups of electric spikes, as

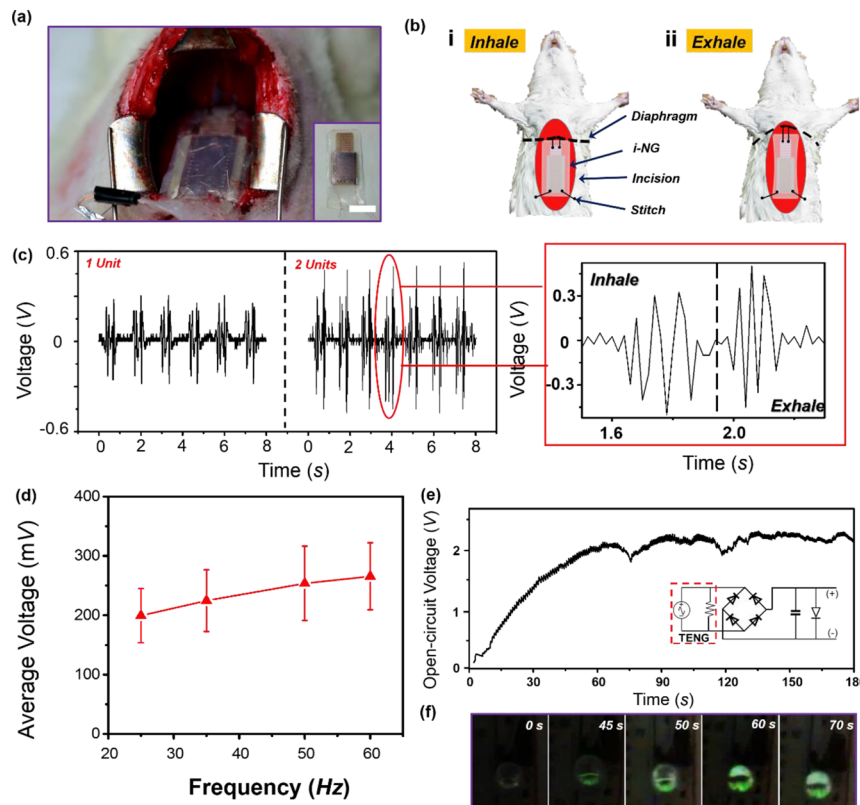


**Figure 4.** In vivo biomechanical energy harvesting and powering performance. (a) Digital image of an i-NG implanted inside the abdominal cavity of a SD rat. The inset is the image of the i-NG device. Scale bar is 1 cm. (b) Working process of the i-NG driven by diaphragm motion during respiration. (c) In vivo voltage outputs measured from i-NGs with a single unit (left) and double unit (right). The right panel is an enlarged voltage output profile within one inhale-exhale cycle. (d) Average in vivo voltage output as a function of rat respiration frequency ( $n = 3$ ). (e) Voltage measured at the LED load as a function of time driven by rat respiration. (f) Series of images recorded on the LED showing the lighting process as the in vivo voltage is building up.

shown in Figure 4c (Video S3). The generation of a group of spikes was because that the mobile layer was pulled back and forth periodically with displacement around 2–4 mm, larger than the periodicity of IDEs ( $600\text{ }\mu\text{m}$ ). Operation of this i-NG required a relatively large displacement as it was specifically designed for harvesting energy from respiration. It may not be applicable to other biomechanical energy sources, such as from bones or joints, where relative movements are hard to obtain.<sup>46,47</sup>

One electrode-pair unit generated a maximum  $V_{\text{pp}}$  of 0.4 V, whereas a two-unit NG nearly doubled the output to  $\sim 0.8$  V. This voltage output was almost the same as those generated in vitro. The negligible output decay from in vitro to in vivo could be attributed to the ultralow Young's modulus of the i-NG, which could be effectively driven by small muscle stretch during the breathing motion. With this ultrastretchable design, the inhalation and exhalation pattern could be clearly distinguished and accurately monitored by the two groups of electrical peaks (Figure 4c). The number of voltage peaks during one respiration cycle was constantly 7–8, well matching the electrode configuration. As the breathing rate of the anesthetized SD rat was kept at  $\sim 45$  times per minute, the average length of voltage envelopes was  $\sim 0.54$  s with an interval of  $\sim 0.76$  s. It was also found that higher breathing rates could lead to higher electrical outputs (Figures 4d and S9), consistent with the reported movement rate and electrical output relationships.<sup>48</sup>

Such a high electrical output was sufficient to drive the green LED as demonstrated in vitro. Without using a rectifier, the respiration of an anesthetized rat could directly light up the LED with obvious blinking because the spiky voltage peaks (Video S4). When connected through a set of rectifier and capacitor, the LED could be stably powered by the anesthetized rat with a breath rate of 45 per minute. As shown in Figure 4e, after experiencing a relatively slow rising process (50–60 s), the potential applied at the LED was stabilized at  $\sim 2.2$  V. The gradual lighting progress of LED was also captured (Figure 4e). The consistent operation of the LED driven by the rat breath was retained over the entire 5 min testing period without any observable degradation of brightness (Video S5). While moderate warping of i-NG would not influence its function (Figure S10), the i-NG exhibited a stable voltage output after more than 1000 breathing cycles or being immersed in 0.9% NaCl saline solution over 24 h (Figure S11 and S12). To the best of our knowledge, this is the first time that small electronics were continuously functioned solely by in vivo biomechanical energy harvested from animal body functions. As for future application to power IMDs, because human body has larger volume, space, and displacement, a significantly enhanced electrical output would be expected once the i-NG was implanted, which might be sufficient to replace batteries.<sup>49</sup> Meanwhile, more stable packaging materials with a similar mechanical property as Ecoflex would be investigated and employed in future work. In addition, biodegradable materials might be considered to replace the chemically stable Silicone, PTFE, and PET films for short-term use of i-NG. It is worth noting that the output voltage of 2.2 V and output power of  $0.1\text{ }\mu\text{W}$  are still insufficient for the operation of most IMDs. A few strategies could be implemented to further improve the output to reach the requirement of practical applications, for example, by integrating more NG units, involving materials with higher tribo-activity, and applying novel surface modifications.

## CONCLUSIONS

In summary, we reported a soft and ultrastretchable i-NG system that can convert slow and discrete muscle movements from breath into a continuous dc output in vivo. The optimized i-NG was built based on the concept of sliding mode TENG with a micrograting electrode configuration. Packaged by a soft silicone elastomer (Ecoflex), an ultralow Young's modulus of  $\sim 45$  kPa was achieved, which was within the range of soft biological tissues. The high biocompatibility of i-NG was validated by measuring the viability of 3T3 fibroblast cells grown on the package materials. The optimal output was obtained from i-NG with  $200\text{ }\mu\text{m}$  electrode width under slow linear motions. The power supply was implanted inside the abdominal cavity of SD rats. Driven by the up and down movements of the diaphragm during breath, a group of multiple voltage output peaks with an amplitude of 0.8 V was obtained in one respiration cycle. After being integrated with a set of rectifier, capacitor, and LED load, the i-NG driven by the in vivo biomechanical energy of rat produced a steady dc output with a voltage up to 2.2 V. This electric output could continuously power the LED without any observable power decay, successfully demonstrating a constant operation of small electronics dc power free of the battery component. Yet there are still several limitations needed to be solved in future research. First, the performance of i-NG would be reduced if the cell or protein absorbed on its surface, and thereby, special processing might need to be added to introduce antifouling property in future clinical applications. Second, more robust encapsulation materials with a similar mechanical property as Ecoflex should be investigated and utilized to ensure the long-term operation. Third, we need to further improve the long-term biocompatibility and biosafety of i-NG materials, particularly the conductive component. Bearing these limitations in mind, this solely biomechanical energy-driven dc micro-power supply will become a very promising solution for the development of self-powered IMDs in the near future.

## EXPERIMENTAL SECTION

**Fabrication of NG.** For the electrode layer preparation, a flexible PET film ( $1.1\text{ cm} \times 2\text{ cm}$ ,  $50\text{ }\mu\text{m}$  thickness, CS Hyde Company, USA) was used as the substrate. An electrode consisting of Cu/Cr (Cu  $280\text{ nm}$  and Cr  $20\text{ nm}$ ) was deposited on the PET substrate by E-beam evaporation (CHA-600). A thin layer of PTFE ( $50\text{ }\mu\text{m}$ , CS Hyde Company, USA) was attached to the PET substrate to cover the electrodes. Dense nanowire arrays were created on the surface of PTFE by the ICP (Plasma-Therm 790 ICP/RIE Etcher) to further enhance the contact area and surface charge density. In a typical ICP process, Ar, O<sub>2</sub>, and CF<sub>4</sub> gases were introduced into the ICP chamber with flow rates of 15.0, 10.0, and 30.0 sccm, respectively. The first power source of 400 W was used to generate a large density of plasma and the other power of 100 W was used to accelerate the plasma ions. The PTFE film was etched for 120 s with a pressure of 10 mTorr. The mobile layer was composed of a central PET film ( $0.8\text{ cm} \times 3\text{ cm}$ ,  $50\text{ }\mu\text{m}$  thickness) sandwiched in between two PTFE films ( $50\text{ }\mu\text{m}$ ). Cu/Cr metal strips (Cu  $280\text{ nm}$  and Cr  $20\text{ nm}$ ) were deposited on the PTFE film by E-beam evaporation. The TENG was assembled by placing an adhesive PET spacer ( $150\text{ }\mu\text{m}$ ) between two electrode layers. Two small holes ( $\sim 2\text{ mm}$  in diameter) were drilled on electrode layers and mobile layer, respectively, for suturing purpose.

**NG Package.** Two glass slides ( $2.5\text{ cm} \times 7.5\text{ cm}$ ) covered with Kapton tape ( $25\text{ }\mu\text{m}$ , CS Hyde Company, USA) were washed by ethanol, isopropanol, and DI water, respectively. Ecoflex 00–30 (Reynolds Advanced Materials, Inc., USA) solution consisting of parts A and B (1A:1B by volume or weight) was spin-coated on the Kapton surface at a speed of 400 rpm for 60 s, followed by curing at  $60^\circ\text{C}$  for

5 min. Two physical masks ( $1.2\text{ cm} \times 1.8\text{ cm}$ , PET) were then placed on the top of each Ecoflex layer. Afterward, an additional layer of Ecoflex was spin-coated on the previous one with physical marks. Curing at room temperature for 5 min, with increased viscosity of the spin-coated elastomer, the physical masks were then taken away without damaging the layer flatness, leaving a patterned cavity behind. After another curing at  $60^\circ\text{C}$  for 1 min, the partially cured elastomers were used to package NG by lamination, and the packaged NG was further cured at  $60^\circ\text{C}$  for 1 h.

**Electrical and Mechanical Characterization.** To characterize the output of NG, the electrode layers were fixed on a stationary stage, while the mobile layer was attached to a moveable stage. Driven by a linear motor, the mobile layer was pulled out and back periodically with a controlled frequency at 1 Hz and a displacement of 4 mm. The voltage was recorded by an Agilent DSO1012A oscilloscope (inter resistance  $1\text{ M}\Omega$ ). The oscilloscope probes were directly connected to the two electrodes of the NG and no additional load resistor was added in between. The short-circuit current was measured by a low-noise current preamplifier (Stanford Research Systems, model SRS70) connected with LabVIEW system in computer. For continuous LED lighting, the open-circuit potentials of the LED and capacitor were measured by the low-noise voltage preamplifier (Stanford Research Systems, model SR560). After i-NG was implanted inside the rats, the in vivo output voltage was also recorded by an Agilent DSO1012A oscilloscope. The mechanical properties of i-NG and the Ecoflex elastomer with equal dimension ( $1.1\text{ cm} \times 3.5\text{ cm} \times 0.8\text{ mm}$ ) were characterized by an RSA III dynamic mechanical analyzer. The strain–stress curves were calculated based on transient force gap tests at room temperature. A rectangular tension/compression geometry was utilized for test.

**Cell Morphology and Immunofluorescence Staining.** After 3T3 cells were cultured on the Ecoflex (00-30) film or cell plates in 24-well plates, the cell morphology was observed directly using an inverted optical microscope (Nikon Eclipse Ti-U, Japan). The cytoskeleton and nucleus were stained with Texas Red-X phalloidin ( $591/608\text{ nm}$ ) and blue fluorescent Hoechst ( $352/461\text{ nm}$ ) (Thermo Fisher Scientific), respectively. The samples were fixed with 2–4% formaldehyde for 15 min and then rinsed three times with prewarmed phosphate-buffered saline. The samples were incubated with Texas Red-X phalloidin ( $100\text{ nM}$ ) and Hoechst ( $50\text{ nM}$ ) for 30 min at  $37^\circ\text{C}$ . After staining, the cells were rinsed with prewarmed buffer for three times and imaged using a Nikon A1RS confocal microscope.

**MTT Assay.** After 3T3 cells were cultured on the packaging film on 24-well plates, MTT assay (Thermo Fisher scientific) was performed to examine cell proliferation. After incubation at  $37^\circ\text{C}$  in a humidified atmosphere with 5%  $\text{CO}_2$  for up to 4 days,  $100\text{ }\mu\text{L}$  of MTT solution was added to each well. After 4 h incubation, the medium was removed and dimethyl sulfoxide ( $500\text{ }\mu\text{L}/\text{well}$ ) was added to dissolve the precipitated fomazan. The optical density ( $n = 3$ ) of the solution was evaluated using a microplate spectrophotometer at a wavelength of 490 nm.

**Implantation of the I-NGs.** All animal experiments were conducted under a protocol approved by the University of Wisconsin Institutional Animal Care and Use Committee. Adult SD rats ( $400\text{--}500\text{ g}$ ) were used for implantation experiment. Anesthesia was first induced by inhalation of 5% isoflurane and maintained with 2% isoflurane. Following anesthesia, rats were fixed in supine position. The abdomen of animals is scrubbed with iodine scrub and then alcohol prior to the surgical procedure. An incision of 3–5 cm was made on the abdomen of animals. I-NG was placed under the diaphragm in the abdomen. The two corners on the upper end of i-NG were sutured near the diaphragm central tendon with two stitches, while another two additional sutures were made inside the abdominal wall near the end of incision to fix the i-NG. After the experiment, the i-NG was taken out and the muscle and skin of rats were sutured. Animals were subsequently euthanized on the same day.

## ASSOCIATED CONTENT

### Supporting Information

The Supporting Information is available free of charge on the ACS Publications website at DOI: [10.1021/acsmami.8b15619](https://doi.org/10.1021/acsmami.8b15619).

Preparation of i-NGs; interdigital electrode image; voltage generation mechanism; equivalent electric circuit; in vitro electrical characterization; more mechanical characterizations of i-NG; 3T3 fibroblast cell culture; surgery process; evaluation of the stability of i-NG; videos; calculation of the equivalent battery capacity; and calculation of the dc output power ([PDF](#))

Continuously lighting LED by i-NG under stretching motion ([MPG](#))

i-NG activated within the rat abdominal cavity by up and down movement of the diaphragm ([MPG](#))

In vivo output of a single-unit i-NG ([MPG](#))

In vivo direct lighting of an LED with blinking ([MPG](#))

Consistent operation of the LED driven by the rat breath ([MPG](#))

## AUTHOR INFORMATION

### Corresponding Authors

\*E-mail: [WCai@uwhealth.org](mailto:WCai@uwhealth.org) (W.C.)

\*E-mail: [xudong.wang@wisc.edu](mailto:xudong.wang@wisc.edu) (X.W.)

### ORCID®

Jun Li: [0000-0002-7498-6736](https://orcid.org/0000-0002-7498-6736)

Weibo Cai: [0000-0003-4641-0833](https://orcid.org/0000-0003-4641-0833)

Xudong Wang: [0000-0002-9762-6792](https://orcid.org/0000-0002-9762-6792)

### Author Contributions

#J.L and L.K contribute equally.

### Notes

The authors declare no competing financial interest.

## ACKNOWLEDGMENTS

This work was primarily supported by the National Institute of Biomedical Imaging and Bioengineering of the National Institutes of Health under Award Number R01EB021336. W.C. thanks the support from the National Institutes of Health (P30CA014520).

## REFERENCES

- (1) Goldberger, Z.; Lampert, R. Implantable Cardioverter-Defibrillators. *JAMA* **2006**, *295*, 809–818.
- (2) Goldstein, D. J.; Oz, M. C.; Rose, E. A. Implantable Left Ventricular Assist Devices. *N. Engl. J. Med.* **1998**, *339*, 1522.
- (3) Navarro, M.; Michiardi, A.; Castano, O.; Planell, J. A. Biomaterials in Orthopaedics. *J. R. Soc. Interface* **2008**, *5*, 1137–1158.
- (4) Amar, A.; Kouki, A.; Cao, H. Power Approaches for Implantable Medical Devices. *Sensors* **2015**, *15*, 28889–28914.
- (5) Bock, D. C.; Marschilok, A. C.; Takeuchi, K. J.; Takeuchi, E. S. Batteries Used to Power Implantable Biomedical Devices. *Electrochim. Acta* **2012**, *84*, 155–164.
- (6) Yang, Z.; Zhou, S.; Zu, J.; Inman, D. High-Performance Piezoelectric Energy Harvesters and Their Applications. *Joule* **2018**, *2*, 642.
- (7) Donelan, J. M.; Li, Q.; Naing, V.; Hoffer, J. A.; Weber, D. J.; Kuo, A. D. Biomechanical Energy Harvesting: Generating Electricity during Walking with Minimal User Effort. *Science* **2008**, *319*, 807–810.
- (8) Gallagher, D.; Heymsfield, S. B.; Heo, M.; Jebb, S. A.; Murgatroyd, P. R.; Sakamoto, Y. Healthy Percentage Body Fat

- Ranges: An Approach for Developing Guidelines Based on Body Mass Index. *Am. J. Clin. Nutr.* **2000**, *72*, 694–701.
- (9) Rolls, B. J. The Role of Energy Density in The Overconsumption of Fat. *J. Nutr.* **2000**, *130*, 268S–271S.
- (10) Kim, M.-K.; Kim, M.-S.; Lee, S.; Kim, C.; Kim, Y.-J. Wearable Thermoelectric Generator for Harvesting Human Body Heat Energy. *Smart Mater. Struct.* **2014**, *23*, 105002.
- (11) Zhang, Z.; He, J.; Wen, T.; Zhai, C.; Han, J.; Mu, J.; Jia, W.; Zhang, B.; Zhang, W.; Chou, X.; Xue, C. Magnetically Levitated-trioboelectric Nanogenerator as A Self-powered Vibration Monitoring Sensor. *Nano Energy* **2017**, *33*, 88–97.
- (12) Li, J.; Kang, L.; Yu, Y.; Long, Y.; Jeffery, J. J.; Cai, W.; Wang, X. Study of Long-term Biocompatibility and Bio-safety of Implantable Nanogenerators. *Nano energy* **2018**, *51*, 728–735.
- (13) Dagdeviren, C.; Yang, B. D.; Su, Y.; Tran, P. L.; Joe, P.; Anderson, E.; Xia, J.; Doraiswamy, V.; Dehdashti, B.; Feng, X.; Lu, B.; Poston, R.; Khalpey, Z.; Ghaffari, R.; Huang, Y.; Slepian, M. J.; Rogers, J. A. Conformal Piezoelectric Energy Harvesting and Storage from Motions of The Heart, Lung, and Diaphragm. *Proc. Natl. Acad. Sci. U.S.A.* **2014**, *111*, 1927–1932.
- (14) Miyake, T.; Haneda, K.; Nagai, N.; Yatagawa, Y.; Onami, H.; Yoshino, S.; Abe, T.; Nishizawa, M. Enzymatic Biofuel Cells Designed for Direct Power Generation from Biofluids in Living Organisms. *Energy Environ. Sci.* **2011**, *4*, 5008–5012.
- (15) Zurbuchen, A.; Pfenniger, A.; Stahel, A.; Stoeck, C. T.; Vandenberghe, S.; Koch, V. M.; Vogel, R. Energy Harvesting from The Beating Heart by A Mass Imbalance Oscillation Generator. *Ann. Biomed. Eng.* **2013**, *41*, 131–141.
- (16) dos Santos, M. P. S.; Ferreira, J. A. F.; Ramos, A.; Simões, J. A. O.; Morais, R.; Silva, N. M.; Santos, P. M.; Reis, M. J. C. S.; Oliveira, T. Instrumented Hip Implants: Electric Supply Systems. *J. Biomech.* **2013**, *46*, 2561–2571.
- (17) Zheng, Q.; Zou, Y.; Zhang, Y.; Liu, Z.; Shi, B.; Wang, X.; Jin, Y.; Ouyang, H.; Li, Z.; Wang, Z. L. Biodegradable Triboelectric Nanogenerator as A Life-time Designed Implantable Power Source. *Sci. Adv.* **2016**, *2*, e1501478.
- (18) Hinchet, R.; Kim, S.-W. Wearable and Implantable Mechanical Energy Harvesters for Self-powered Biomedical Systems. *ACS Nano* **2015**, *9*, 7742–7745.
- (19) Ma, Y.; Zheng, Q.; Liu, Y.; Shi, B.; Xue, X.; Ji, W.; Liu, Z.; Jin, Y.; Zou, Y.; An, Z.; Zhang, W.; Wang, X.; Jiang, W.; Xu, Z.; Wang, Z. L.; Li, Z.; Zhang, H. Self-Powered, One-Stop, and Multifunctional Implantable Triboelectric Active Sensor for Real-Time Biomedical Monitoring. *Nano Lett.* **2016**, *16*, 6042–6051.
- (20) Zheng, Q.; Zhang, H.; Shi, B.; Xue, X.; Liu, Z.; Jin, Y.; Ma, Y.; Zou, Y.; Wang, X.; An, Z.; Tang, W.; Zhang, W.; Yang, F.; Liu, Y.; Lang, X.; Xu, Z.; Li, Z.; Wang, Z. L. In Vivo Self-Powered Wireless Cardiac Monitoring via Implantable Triboelectric Nanogenerator. *ACS Nano* **2016**, *10*, 6510–6518.
- (21) Zheng, Q.; Shi, B.; Fan, F.; Wang, X.; Yan, L.; Yuan, W.; Wang, S.; Liu, H.; Li, Z.; Wang, Z. L. In Vivo Powering of Pacemaker by Breathing-driven Implanted Triboelectric Nanogenerator. *Adv. Mater.* **2014**, *26*, 5851–5856.
- (22) Wang, M.; Zhang, J.; Tang, Y.; Li, J.; Zhang, B.; Liang, E.; Mao, Y.; Wang, X. Air Flow-Driven Triboelectric Nanogenerators for Self-Powered Real-Time Respiratory Monitoring. *ACS Nano* **2018**, *12*, 6156.
- (23) Li, J.; Wang, X. Research Update: Materials Design of Implantable Nanogenerators for Biomechanical Energy Harvesting. *APL Mater.* **2017**, *5*, 073801.
- (24) Yu, Y.; Sun, H.; Orbay, H.; Chen, F.; England, C. G.; Cai, W.; Wang, X. Biocompatibility and In Vivo Operation of Implantable Mesoporous PVDF-based Nanogenerators. *Nano Energy* **2016**, *27*, 27S–281.
- (25) Mahmud, M. A. P.; Huda, N.; Farjana, S. H.; Asadnia, M.; Lang, C. Recent Advances in Nanogenerator-Driven Self-Powered Implantable Biomedical Devices. *Adv. Energy Mater.* **2018**, *8*, 1701210.
- (26) Mao, Y.; Zhang, N.; Tang, Y.; Wang, M.; Chao, M.; Liang, E. A Paper Triboelectric Nanogenerator for Self-powered Electronic Systems. *Nanoscale* **2017**, *9*, 14499–14505.
- (27) Kim, D. H.; Shin, H. J.; Lee, H.; Jeong, C. K.; Park, H.; Hwang, G.-T.; Lee, H.-Y.; Joe, D. J.; Han, J. H.; Lee, S. H.; Kim, J.; Joung, B.; Lee, K. J. In Vivo Self-Powered Wireless Transmission Using Biocompatible Flexible Energy Harvesters. *Adv. Funct. Mater.* **2017**, *27*, 1700341.
- (28) Yu, D. Y. W.; Spaepen, F. The Yield Strength of Thin Copper Films on Kapton. *J. Appl. Phys.* **2004**, *95*, 2991–2997.
- (29) Agag, T.; Koga, T.; Takeichi, T. Studies on thermal and mechanical properties of polyimide-clay nanocomposites. *Polymer* **2001**, *42*, 3399–3408.
- (30) Xie, Y.; Wang, S.; Niu, S.; Lin, L.; Jing, Q.; Yang, J.; Wu, Z.; Wang, Z. L. Grating-Structured Freestanding Triboelectric-Layer Nanogenerator for Harvesting Mechanical Energy at 85% Total Conversion Efficiency. *Adv. Mater.* **2014**, *26*, 6599–6607.
- (31) Zhu, G.; Zhou, Y. S.; Bai, P.; Meng, X. S.; Jing, Q.; Chen, J.; Wang, Z. L. A Shape-Adaptive Thin-Film-Based Approach for 50% High-Efficiency Energy Generation Through Micro-Grating Sliding Electrification. *Adv. Mater.* **2014**, *26*, 3788–3796.
- (32) Morber, J. R.; Wang, X.; Liu, J.; Snyder, R. L.; Wang, Z. L. Wafer-Level Patterned and Aligned Polymer Nanowire/Micro- and Nanotube Arrays on any Substrate. *Adv. Mater.* **2009**, *21*, 2072–2076.
- (33) Wang, S.; Niu, S.; Yang, J.; Lin, L.; Wang, Z. L. Quantitative Measurements of Vibration Amplitude Using A Contact-mode Freestanding Triboelectric Nanogenerator. *ACS Nano* **2014**, *8*, 12004–12013.
- (34) Jiang, T.; Chen, X.; Han, C. B.; Tang, W.; Wang, Z. L. Theoretical Study of Rotary Freestanding Triboelectric Nanogenerators. *Adv. Funct. Mater.* **2015**, *25*, 2928–2938.
- (35) Niu, S.; Wang, S.; Liu, Y.; Zhou, Y. S.; Lin, L.; Hu, Y.; Pradel, K. C.; Wang, Z. L. A Theoretical Study of Grating Structured Triboelectric Nanogenerators. *Energy Environ. Sci.* **2014**, *7*, 2339–2349.
- (36) Ma, Y.; Pharr, M.; Wang, L.; Kim, J.; Liu, Y.; Xue, Y.; Ning, R.; Wang, X.; Chung, H. U.; Feng, X. Soft Elastomers with Ionic Liquid-Filled Cavities as Strain Isolating Substrates for Wearable Electronics. *Small* **2017**, *13*, 1602954.
- (37) Shepherd, R. F.; Ilievski, F.; Choi, W.; Morin, S. A.; Stokes, A. A.; Mazzeo, A. D.; Chen, X.; Wang, M.; Whitesides, G. M. Multigait soft robot. *Proc. Natl. Acad. Sci. U.S.A.* **2011**, *108*, 20400–20403.
- (38) Martinez, R. V.; Branch, J. L.; Fish, C. R.; Jin, L.; Shepherd, R. F.; Nunes, R. M. D.; Suo, Z.; Whitesides, G. M. Robotic Tentacles with Three-Dimensional Mobility Based on Flexible Elastomers. *Adv. Mater.* **2013**, *25*, 205–212.
- (39) Egorov, V.; Tsuryupa, S.; Kanilo, S.; Kogit, M.; Sarvazyan, A. Soft Tissue Elastometer. *Med. Eng. Phys.* **2008**, *30*, 206–212.
- (40) Akhtar, R.; Sherratt, M. J.; Cruickshank, J. K.; Derby, B. Characterizing the Elastic Properties of Tissues. *Mater. Today* **2011**, *14*, 96–105.
- (41) Kot, B. C. W.; Zhang, Z. J.; Lee, A. W. C.; Leung, V. Y. F.; Fu, S. N. Elastic Modulus of Muscle and Tendon with Shear Wave Ultrasound Elastography: Variations with Different Technical Settings. *PLoS One* **2012**, *7*, e44348.
- (42) Bae, W. J.; Choi, J. B.; Kim, K. S.; Kim, S. J.; Cho, H. J.; Ha, U. S.; Hong, S. H.; Lee, J. Y.; Kim, S. W. AB168. Evaluation of The Biocompatibility of Packing Materials for a Catheter. *Transl. Androl. Urol.* **2015**, *4*, AB168.
- (43) Park, G.; Chung, H.-J.; Kim, K.; Lim, S. A.; Kim, J.; Kim, Y.-S.; Liu, Y.; Yeo, W.-H.; Kim, R.-H.; Kim, S. S.; Kim, J.-S.; Jung, Y. H.; Kim, T.-i.; Yee, C.; Rogers, J. A.; Lee, K.-M. Immunologic and Tissue Biocompatibility of Flexible/stretchable Electronics and Optoelectronics. *Adv. Healthcare Mater.* **2014**, *3*, 515–525.
- (44) Ogneva, I. V.; Lebedev, D. V.; Shenkman, B. S. Transversal Stiffness and Young's Modulus of Single Fibers from Rat Soleus Muscle Probed by Atomic Force Microscopy. *Biophys. J.* **2010**, *98*, 418–424.

(45) Defranchi, E.; Bonaccurso, E.; Tedesco, M.; Canato, M.; Pavan, E.; Raiteri, R.; Reggiani, C. Imaging and Elasticity Measurements of The Sarcolemma of Fully Differentiated Skeletal Muscle Fibres. *Microsc. Res. Tech.* **2005**, *67*, 27–35.

(46) dos Santos, M. P. S.; Marote, A.; Santos, T.; Torrão, J.; Ramos, A.; Simões, J. A. O.; da Cruz e Silva, O. A. B.; Furlani, E. P.; Vieira, S. I.; Ferreira, J. A. F. New Cosurface Capacitive Stimulators for The Development of Active Osseointegrative Implantable Devices. *Sci. Rep.* **2016**, *6*, 30231.

(47) Bonmassar, G.; Lee, S. W.; Freeman, D. K.; Polasek, M.; Fried, S. I.; Gale, J. T. Microscopic Magnetic Stimulation of Neural Tissue. *Nat. Commun.* **2012**, *3*, 921.

(48) Niu, S.; Liu, Y.; Wang, S.; Lin, L.; Zhou, Y. S.; Hu, Y.; Wang, Z. L. Theory of Sliding-Mode Triboelectric Nanogenerators. *Adv. Mater.* **2013**, *25*, 6184–6193.

(49) Whitelaw, W. A. Shape and Size of The Human Diaphragm in vivo. *J. Appl. Physiol.* **1987**, *62*, 180–186.